 CMES, vol.6, no.3, pp.295-308, 2004

Calculation of J-Integral and Stress Intensity Factors using the Material Point Method

Y. Guo[1] **and J. A. Nairn**[1]

Abstract: The Material Point Method (MPM), which is a particle-based, meshless method that discretizes material bodies into a collection of material points (the particles), is a new method for numerical analysis of dynamic solid mechanics problems. Recently, MPM has been generalized to include dynamic stress analysis of structures with explicit cracks. This paper considers evaluation of crack-tip parameters, such as J-integral and stress intensity factors, from MPM calculations involving explicit cracks. Examples for both static and dynamic problems for pure modes I and II or mixed mode loading show that MPM works well for calculation of fracture parameters. The MPM results agree well with results obtained by other numerical methods and with analytical solutions.

keyword: Material point method (MPM), dynamic fracture, J integral, stress intensity factor.

1 Introduction

Many experimental methods are available for investigating the dynamic fracture properties of materials and structures. Because of the very short time scales for dynamic fracture events, it is difficult to directly measure physical fracture quantities such as J-integral, energy release rates, or stress intensity factors, particularly in opaque specimens or structures of practical interest. Computational calculations have the potential to overcome the difficulties associated with interpreting dynamic fracture mechanics experiments. The approach would be to use calculations to evaluate physical fracture quantities of a dynamic crack tip at any instant of time during the experiment. The advancement of dynamic fracture mechanics, therefore, relies heavily on advancements of numerical fracture methods.

The numerical analysis of dynamic fracture is often considered as a package using various numerical methods, but the problem actually partitions into three distinct problems that can be solved independently:

1. **Analysis of explicit cracks**: The first problem is to develop numerical methods that can evaluate stresses and displacements around explicit cracks.

2. **Calculation of fracture parameters**: Once explicit crack analysis is possible, each numerical method needs techniques to evaluate key crack-tip parameters such as J integral, energy release rate, stress intensity factors, or various other local crack-tip properties.

3. **Prediction and inclusion of crack propagation**: Once crack tip parameters are available, the next issue is to predict what conditions are required for crack propagation and in what direction the crack will propagate. This problem is a material science problem and not dependent on the particular numerical method chosen for analysis. For a particular numerical method to be effective, however, it should be capable of modeling crack propagation in arbitrary directions and continuing the analysis as the crack grows.

One of the earliest applications of numerical methods to dynamic fracture problems is the finite difference method (FDM) developed by Chen and Wilkens (1977). Later, finite element analysis (FEA) became the preferred numerical tool [Nishioka and Atluri (1983), Nishioka (1995), Nishioka (1983), Nishioka (1997), Nishioka, Tokudome, and Kinoshita (2001), Nishioka and Stan (2003)]. The analysis of explicit cracks in FEA is easily handled by introducing cracks in the mesh, but FEA can have difficulty dealing with crack surface contact. FEA can evaluate fracture parameters by methods such as crack closure [Rybicki and Kanninen (1977)], but encounters difficulties in coping with crack propagation, especially crack

[1] Material Science and Engineering, University of Utah, Salt Lake City, Utah 84112, USA

propagation in arbitrary directions [Nishioka, Tokudome, and Kinoshita (2001)]. Another problem of FEA is difficulty with problems having large deformations or rotations, where the finite element mesh could become distorted requiring re-meshing methods and causing a great decrease in calculation efficiency. A dual boundary integration method was developed to obtain dynamic stress intensity factors [Wen, Aliabadi, and Rooke (1998)]. Because the crack opening displacements are used to calculate stress intensity in this method, attention must be paid, and some techniques have to be used, to improve the accuracy of crack opening displacements near crack tips before stress intensity factors are reliable. To avoid mesh problems of FEA and to better handle crack propagation in arbitrary directions, some meshless methods [Atluri and Shen (2002), Han and Atluri (2003b)] have been developed for dynamic fracture analysis [Belytschko, Lu, and Gu (1994), Organ, Fleming, and Belytschko (1996), Batra and Ching (2002), Han and Atluri (2003a)], as well as a cell method [Ferretti (2003)]. For example, Batra and Ching (2002) extended the Meshless Local Petrov-Galerkin (MLPG) method for inclusion of cracks and evaluation of stress intensity factors (problems 1 and 2 above). As in other meshless methods, however, the inclusion of cracks in MLPG required definition of particle "influence" zones near crack surfaces to be able to handle explicit cracks. These influence zones have to be evaluated by approximate node-visibility or stress-diffraction rules [Organ, Fleming, and Belytschko (1996), Batra and Ching (2002)]. Furthermore, it might be hard to incorporate contact algorithms for handling crack surface contact in MLPG.

A new particle-based method, called the material point method (MPM), is developing into a new numerical tool for solving dynamic solid mechanics problems [Sulsky, Chen, and Schreyer (1994), Sulsky, Zhou, and Schreyer (1995), Sulsky and Schreyer (1996), Nairn (2003), Bardenhagen, Guilkey, Roessig, Brackbill, Witzel, and Foster (2001), Bardenhagen and Kober (2004)]. In the material point method, the object being analyzed is discretized into a collection of particles or material points. As the dynamic analysis proceeds, the solution is tracked on the particles by updating all required properties such as position, velocity, acceleration, stress state, *etc.*. At each time step, the equations of motion for the particles are solved on a background grid; this solution is used to update the particles and the background mesh can be discarded or reused for the next time step in its initial, undistorted form. This combination of Lagrangian and Eulerian methods has proven useful for solving solid mechanics problems, particularly for problems with large deformations and rotations. Despite the use of a background mesh, a recent derivation of a generalized MPM method [Bardenhagen and Kober (2004)] shows that MPM is a Petrov-Galerkin method having more in common with other meshless methods than with finite element methods.

The standard derivation of MPM enforces continuous displacements. Although such an analysis can handle some fracture properties with special symmetries [Tan and Nairn (2002)], it can not handle arbitrary explicit cracks. Recently we have developed a new MPM algorithm called CRAMP for cracks in material point calculations [Nairn (2003)]. This new algorithm solves the first problem in numerical analysis of fracture on the analysis of explicit cracks. It handles cracks naturally with the full accuracy of MPM. In other words, it is comparable to FEA in the ease of including explicit cracks and has advantages over other meshless methods by not requiring crack approximations such as node-visibility or stress-diffraction rules [Organ, Fleming, and Belytschko (1996), Batra and Ching (2002)]. CRAMP may also have advantages over both FEA and other meshless methods in its ability to fully model crack surface contact including frictionless sliding, sliding with friction, or stick conditions [Nairn (2003), Bardenhagen, Guilkey, Roessig, Brackbill, Witzel, and Foster (2001), Bardenhagen, Brackbill, and Sulsky (2000)].

Now that MPM/CRAMP can handle explicit cracks, the goal of this paper was to address the second problem in numerical analysis of fracture or to develop MPM methods for calculating fracture parameters and to verify that MPM is suitable method for such calculations. We found that MPM is well-suited to efficient and accurate calculation of J integral around cracks. By tracking crack opening displacements, it was further possible to convert J-integral results into mode I and mode II stress intensity factors. These results suggest that MPM is an excellent candidate for the last fracture problem or the implementation of failure criteria to predict both crack growth and growth direction. Because the MPM solution and the crack definition are defined on particles, it is easy to implement crack propagation in arbitrary directions. Perhaps MPM will combine the algorithmic efficiencies of

FEA for analysis of explicit cracks with the flexibility of meshless methods for describing arbitrary crack paths.

2 Numerical Methods

2.1 MPM Calculations with Explicit Cracks

The material point method (MPM), as originally derived, extrapolates particle information to a background grid for solution of the equations of motion [Sulsky, Chen, and Schreyer (1994), Sulsky, Zhou, and Schreyer (1995), Sulsky and Schreyer (1996)]. Because this extrapolation enforces continuous velocities on the grid, the original method could not accommodate cracks which are mathematically described by velocity or displacement discontinuities. To extend MPM to crack problems, we developed a new algorithm called CRAMP for cracks in material point method calculations. This section gives a brief review of the CRAMP algorithm; the detailed algorithm is in Nairn (2003). The key difference in MPM with cracks are:

1. To account for cracks, modify the MPM extrapolation of particle information to the grid to allow nodes near cracks to have multiple velocity fields. The separate velocity fields contain information for the solution on opposite sides of the cracks.

2. To determine which nodes need multiple velocity fields, cracks are introduced in the problem by additional mass-less particles. In $2D$ problems the additional particles are connected by line segments to define the crack path. In $3D$ problems, crack definition requires defining a crack surface [Guo and Nairn (2004)]. When extrapolating any particle p to node i, a line is drawn from the particle to the node and each particle/node pair is assigned a field number $\nu(p,i)$ which is $\nu(p,i)=0$ if the line crosses no crack (*i.e.*, conventional MPM), $\nu(p,i)=1$ if the line crosses a crack and the particle is above the crack, or $\nu(p,i)=2$ if the line crosses the crack and the particle is below the crack. The concept of "above" or "below" the crack is relative to a coordinate system with the crack tip at the origin and the crack direction in the negative x direction (or crack plane in the negative x-z plane in 3D problems).

3. Solve the equations of motion by conventional MPM methods, but for cracks with multiple velocity fields, solve the equations of motion for each velocity field separately.

4. To prevent non-physical overlap at displacement discontinuities, implement contact rules at all nodes with multiple velocity fields [Nairn (2003), Bardenhagen, Guilkey, Roessig, Brackbill, Witzel, and Foster (2001)].

5. Using the nodal solutions, interpolate back to the particles and update the solution on the particles such as particle stress, strain, velocity, and displacement. The interpolation back to the particles uses the appropriate velocity field as determined in step 2.

6. Finally, update the crack position within the body. In the previous paper [Nairn (2003)], this step updated the position of all crack particles by using the center-of-mass velocity field. In this work, we added an extra update of crack information to track crack surfaces or crack opening displacements (see below).

2.2 CRAMP-Modified MPM Equations

Consider a solid body containing a crack subjected to body force per unit volume $\vec{B}$ and surface force $\vec{T}$ which has been resolved into forces applied directly to particles, $\vec{F}_p$ (see Fig. 1). The virtual work principle for the system can be expressed by [Cook, Malkus, and Plesha (1989)]:

$$\int_V \vec{B}\cdot\delta\vec{u}\,dV+\sum_p \vec{F}_p\cdot\delta\vec{u}=\int_V \vec{\sigma}\cdot\delta\vec{\varepsilon}\,dV + \int_V \rho\frac{d^2\vec{u}}{dt^2}\cdot\delta\vec{u}\,dV+\int_V d_k\frac{d\vec{u}}{dt}\cdot\delta\vec{u}\,dV \qquad (1)$$

where ρ is density, d_k is a damping coefficient, $\vec{u}$, $\vec{\varepsilon}$, and $\vec{\sigma}$ are the displacement, strain, and stress, respectively, and t is time. The term $\delta\vec{u}$ denotes an arbitrary virtual displacement that is allowed physically. In MPM, the body is divided into a collection of particles each assigned a mass of m_p consistent with the material density. All the variables needed to solve the problem (*e.g.*, position, velocity, stress, *etc.*) are carried on the particles. To solve the equations of motion for the particles, MPM uses a background computational grid, as shown in Fig. 1. Interpolating particle properties and virtual displacement to the grid and numerically evaluating the integrals using

the particles as integration points, the virtual work equation reduces to separate equations for nodal accelerations of each velocity field ($\vec{a}_{i,\nu(p,i)}$):

$$\vec{a}_{i,\nu(p,i)} = \frac{\vec{f}^{tot}_{i,\nu(p,i)}}{M^L_{i,\nu(p,i)}} \tag{2}$$

where $\vec{f}^{tot}_i$ are the total nodal forces, and M^L_i are the lumped nodal masses. The second subscript $\nu(p,i) = 0, 1,$ or 2 corresponds to each of the three possible velocity fields in the CRAMP algorithm. Although each node has three potential velocity fields, only nodes near cracks will have more than the single $\nu(p,i) = 0$ field. For the example, in Fig. 1 only the nodal points along the crack plane will have multiple velocity fields. Furthermore, even nodes near cracks will have at most two velocity fields that correspond to information extrapolated from opposite sides of the crack near that node. (Note: although the crack plane in Fig. 1 is shown along grid lines, the crack particles will numerically reside on one side or the other from the grid line. Although issues can arise due to numerical round off, they can be avoided by careful selection of the line-crossing algorithm [Nairn (2003)].)

The remaining MPM equations [Sulsky, Chen, and Schreyer (1994)] all need modification to account for the possibility of multiple velocity fields. The lumped mass matrix at a node i is

$$M^L_{i,k} = \sum_p m_p N_{i,p} \delta_{k,\nu(p,i)} \quad (k = 0,1,2) \tag{3}$$

The total nodal forces are the sum of the external forces and the internal forces:

$$\vec{f}^{tot}_{i,k} = \vec{f}^{ext}_{i,k} + \vec{f}^{int}_{i,k} \quad (k = 0,1,2) \tag{4}$$

where

$$\vec{f}^{ext}_{i,k} = \sum_p \vec{F}_p N_{i,p} \delta_{k,\nu(p,i)} - \frac{d_k}{\rho} \sum_p m_p \vec{v}_p N_{i,p} \delta_{k,\nu(p,i)} \tag{5}$$

$$\vec{f}^{int}_{i,k} = \sum_p m_p \left(\vec{B}^s_p N_{i,p} - \vec{\sigma}^s_p \cdot \nabla N_{i,p} \right) \delta_{k,\nu(p,i)} \tag{6}$$

for $k = 0,1,2$ and where superscript s denotes a specific quantity, $N_{i,p} = N_i(\vec{x}_p)$ and $\nabla N_{i,p} = \nabla N_i(\vec{x}_p)$ are the shape function and its' gradient for node i at the position of particle p ($\vec{x}_p$), $\vec{v}_p$ is the particle velocity, and $\delta_{k,\nu(p,i)}$ is Kronecker delta or 1 if $k = \nu(p,i)$ and 0 otherwise.

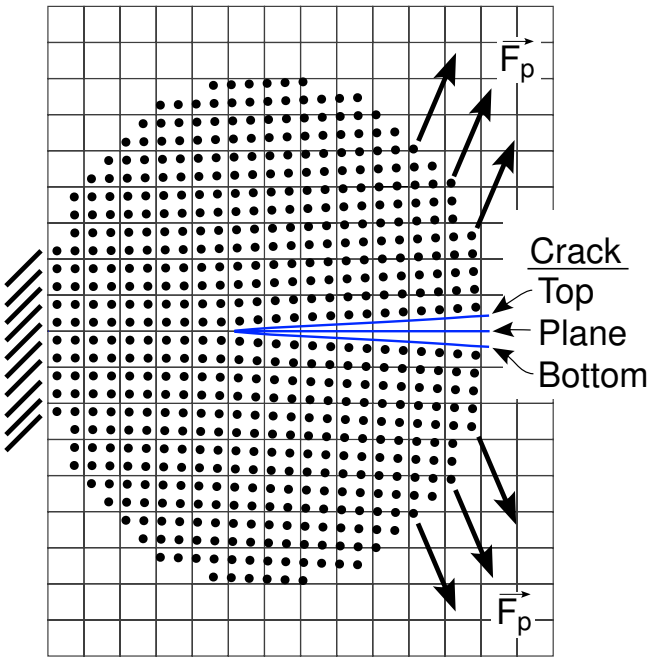

Figure 1 : Discretization of a solid object with a crack into material points or particles. The grid is the background mesh for MPM calculations. The CRAMP algorithm tracks the crack as mass-less particles connected by line segments; it also tracks the top and bottom crack surfaces to provide information about crack opening displacement.

Once nodal velocities have been updated, the nodal state is interpolated back to the particles to update their velocity, position, stress, strain, *etc.*. In CRAMP, the interpolation is done using the proper velocity field for each particle near a crack [Nairn (2003)]. Finally, the center-of-mass velocity for each particle in the definition of the crack plane is used to update the crack position. A new feature added to CRAMP in this work was to additionally use the separate velocity fields to track the positions of the crack surfaces. Initially the crack is assumed to be closed. During each MPM time step, the separate velocity fields near cracks are used to update the positions of the top and bottom surfaces of the crack. Figure 1 shows a crack "Plane" which is defined by a collection of massless particles connected by line segments. The "Top" and "Bottom" crack surfaces are tracked as displacements from that crack plane during the analysis. The crack opening displacement information is useful in partitioning the stress state into mode I and mode II stress intensity factor.

An additional use for tracking crack opening displacements might be to implement numerical methods for detection of crack contact. Prior MPM methods for detecting two-body or crack contact have been based on surface velocities or on nodal volumes or on both [Nairn (2003), Bardenhagen, Guilkey, Roessig, Brackbill, Witzel, and Foster (2001), Bardenhagen, Brackbill, and Sulsky (2000)]. Because contact detection is done for grid nodes with multiple velocity fields while crack opening displacements are tracked on the massless crack particles, it is more efficient to use grid methods rather than the new crack opening displacement information. The calculations in this paper have thus continued to use the grid- and volume-based method described in Nairn (2003). By monitoring the crack opening displacement on the crack particles, we could confirm that the grid-based crack-contact detection algorithm worked well for all examples in this paper. We have experimented with displacement-based methods for crack-contact detection that extrapolates displacements within the two velocity fields to grid nodes and detects contact based on relative normal displacements. This approach works well, but requires an extra extrapolation for nodal displacement information.

In typical problems with cracks, only a few nodes near cracks will actually have multiple velocity fields and thus the CRAMP algorithm is very efficient. The computational overhead for cracks in 2D problems is typically about 10% [Nairn (2003)]. Additionally, MPM with cracks may have advantages over other particle-based or meshless methods for inclusion of explicit cracks. The CRAMP algorithm is an *exact* MPM representation of cracks or displacement discontinuities analogous to the fact that the addition of cracks to an FEA mesh provides an *exact* FEA representation of discontinuities. In contrast, other meshless methods can only include displacement discontinuities by approximate methods such as node-visibility rules [Belytschko, Lu, and Gu (1994)] or stress-diffraction parameters [Organ, Fleming, and Belytschko (1996)].

3 *J*-integral and Stress Intensity Factor Calculations in MPM

The CRAMP algorithm modification to MPM has extended MPM to include explicit cracks and thereby determine stress fields, displacements, *etc.*, near crack tips. To implement fracture mechanics models for crack propagation, the next step is to calculate fracture parameters for crack tips such as energy release rate and stress intensity factors. This section describes MPM calculations of J-integral around a crack tip and partitioning of the results into mode I and mode II stress intensity factors.

The J-integral, as a key fracture parameter, was introduced by Cherepanov (1967) and Rice (1968). Although the first derivation of J-integral was for quasi-static problems with no kinetic energy, the concept can be extended to dynamic problems by including kinetic energy. The definition of dynamic J-integral components (J_m for $m = 1,2$) at a crack tip (see Fig. 2) is [Nishioka (1995), Cherepanov (1979)],

$$J_m = \lim_{\varepsilon\to 0}\int_{\Gamma_\varepsilon}\left[\Big(W+K\Big)n_m - \sigma_{ij}n_j\frac{\partial u_i}{\partial x_m}\right]d\Gamma \qquad (7)$$

$$= \int_{\Gamma}\left[\Big(W+K\Big)n_m - \sigma_{ij}n_j\frac{\partial u_i}{\partial x_m}\right]d\Gamma + \int_{A(\Gamma)}\rho\left[\frac{\partial^2 u_i}{\partial t^2}\frac{\partial u_i}{\partial x_m} - \frac{\partial u_i}{\partial t}\frac{\partial^2 u_i}{\partial t\partial x_m}\right]dA \qquad (8)$$

where W and K are the stress-work density and kinetic energy density, respectively, σ_{ij} are stresses, u_i are displacements (accordingly, $\partial u_i/\partial x_m$ are the components of displacement gradients, $\partial u_i/\partial t$ is velocity, and $\partial^2 u_i/\partial t^2$ is acceleration), n_m are components of the unit normal vector to the J-integral contour (Γ or Γ_ε), ρ is density, and repeated indices i and j are summed. The energy terms are

$$W = \sigma_{ij}d\varepsilon_{ij} \quad \text{and} \quad K = \frac{1}{2}\rho\dot{u}_i\dot{u}_i \qquad (9)$$

where ε_{ij} are strains. The Γ and Γ_ε are line integrals along contours around the crack tip. The $A(\Gamma)$ integral is an integral over the area enclosed by the contour.

For static problems, the area integral drops out and the result is path independent for any crack tip contour (Γ or Γ_ε) [Rice (1968)]. This path independence is lost for dynamic problems because the transmission of energy to different paths depends on the time stress waves reach the path. There are two solutions to the problem as expressed by the two results for J_m above [Nishioka (1995)]. In the first solution (Eq. 7), J_m is calculated in the limit of a small contour Γ_ε. In this limit the components of the J-integral are well defined because the $A(\Gamma)$ integral becomes negligible. The second solution (Eq. 8) can be used for an arbitrary contour, Γ, provided an extra term,

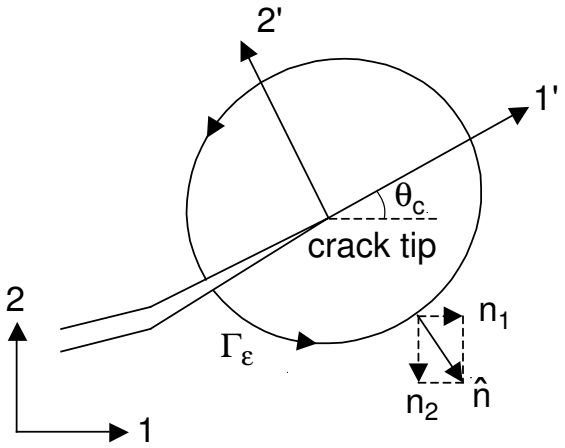

Figure 2 : Nomenclature and coordinates for terms used in the J-integral calculation. The 1 and 2 axes are global x and y axes. The $1'$ and $2'$ axes are aligned with the current crack direction. The contour Γ_ε starts on one crack surface and proceeds counter-clockwise to the opposite crack surface.

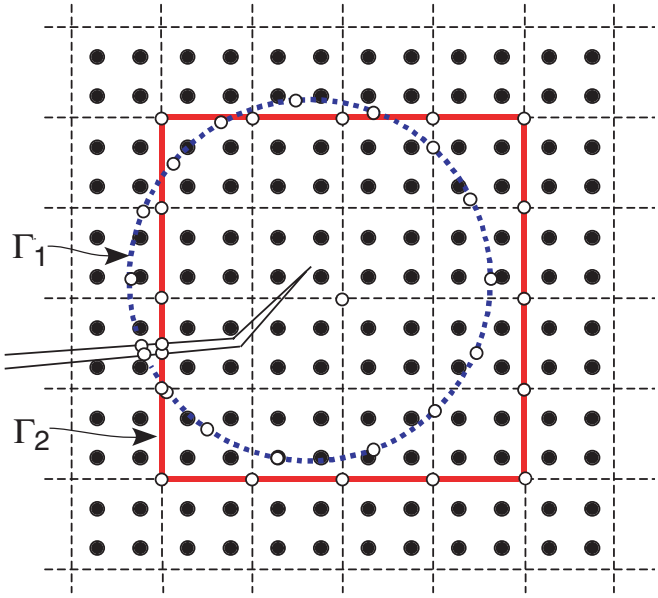

Figure 3 : Two possible J-integral contours around a crack tip in MPM calculations. The calculations in this paper all used the rectangular path for computational efficiency. This path is centered on the node nearest to the crack tip and extends 2 cells in each direction from that node.

which integrates the area enclosed by Γ or $A(\Gamma)$, is included. The two combined terms are independent of Γ [Nishioka (1995)], but the calculation of J is no longer a single line integral. Most of the results in this paper used the first equation by numerical integration over a path close to the crack tip. The effect of path size, using an example when the second term is needed, was also investigated.

Once the components of the J-integral are evaluated, the total energy release rate for crack growth in elastic materials (linear or non-linear) is given by [Nishioka (1983)]:

$$G = J_1 \cos\theta_c + J_2 \sin\theta_c \tag{10}$$

where θ_c is the crack propagation angle measured from x-axis in the global coordinates (see Fig. 2). J_1 and J_2 are components of J integral, as evaluated in Eq. 7.

Figure 3 shows two potential J-integral contours around a crack tip. The curve Γ_1 is a circular path centered on the crack tip. The curve Γ_2 is a rectangular path that follows grid lines in the background MPM mesh; it is centered on the node nearest to the crack tip. Because J-integral is path-independent in the limit of small path length or by inclusion of the volume integral, the J-integral contour can be chosen arbitrarily. All calculations in this paper were done with the rectangular path. By using a contour that follows mesh lines in the background grid, the numerical integration to find J integral was more efficient.

Rectangular paths are denoted here as $n \times m$ paths where n and m are the distance from the central node to the contour in the x and y directions. All paths where chosen to be square ($n = m$). The path in Fig. 3 is a 2×2 contour.

The numerical J-integral calculations proceeded as follows. First, to get terms required for the contour integral, all needed terms from the current particle states were extrapolated to the nodes on the background mesh. The nodal values were extrapolated by standard MPM methods using

$$f_{i,k} = \frac{\sum_p m_p f_p N_{i,p} \delta_{k,\mathrm{v}(p,i)}}{M^L_{i,k}} \quad (k = 0,1,2) \tag{11}$$

where f represents any property; $f_{i,k}$ are the nodal values, and f_p are the values on the particles. The extrapolation to get displacement gradients used particle strain (*e.g.*, $\partial u_1/\partial x = \varepsilon_{xx}$); to include cross-derivatives, the code separately tracked $\partial u_1/\partial y$ and $\partial u_2/\partial x$ on particles rather than just the sum or shear strain γ_{xy}. Importantly, the extrapolation must preserve the multiple velocity fields ($k = 0,1,2$) to provide information for the two sides of the crack. Next, the node closest to the crack tip was located and a rectangular path centered on that node was

calculated. For reasonably behaved cracks, this path will cross the crack once. That crossing point was located, two nodes were placed at the cross-over point, and the path was split to create a contour starting on one crack surface and ending on the opposite crack surface. The nodal values for stresses, energies, displacements, *etc.*, for the two new nodes were found by interpolation between the two neighboring background mesh nodes on the rectangular path. The neighboring nodes will always have two velocity fields. The interpolation of these two velocity fields gave two separate results resulting in one new node that corresponded to the stress state on one surface of the crack while the other one corresponded to the stress state on the opposite side of the crack. Finally, assuming there were n_J nodes (or $n_J - 1$ segments) along the final J-integral contour, the components of the J-integral were numerically integrated using the midpoint rule:

$$J_m = \sum_{i=1}^{n_J-1} \left(F_m^{(i)} + F_m^{(i+1)} \right) \frac{\Delta_i}{2} \quad (m = 1,2) \tag{12}$$

where Δ_i is the length of segment i and the integrand at each node, $F_m^{(i)}$, is:

$$F_m^{(i)} = \left(W_{i,k} + K_{i,k} \right) n_m - \vec{\sigma}_{i,k} \hat{n} \cdot \frac{\partial \vec{u}_{i,k}}{\partial x_m} \tag{13}$$

Here subscript i denotes nodal value while subscript k denotes the appropriate velocity field. The integration starts on one crack surface with the velocity field appropriate for that crack surface (velocity field for particles above or below the crack depending on crack orientation). Whenever nodes have multiple velocity fields, the initial velocity field was used for the first half of the nodes while the opposite velocity field was used for the later half of the segments. In practice, nodes near the middle on the contour had single velocity fields and there was never ambiguity of the appropriate velocity field.

For calculations using Eq. 8, the second term was evaluated by numerical integration over the area enclosed by the rectangular path. The particles enclosed by the path were used as equally-weighted integration points. The current particle properties for velocity, displacement gradient, and acceleration were used to calculate the integrand. The representation of the solution on the particles does not have separate velocity fields, but, the particle states automatically provide the proper result for the area integration.

The energy release rate, G, was calculated by Eq. 10; the angle θ_c for the calculation was found from the angle of the line segment at the crack tip. To partition total energy release rate, G, into mode I and mode II components, the G results were converted into mode I and mode II stress intensity factors — K_I and K_{II}. The calculation of G is valid for any elastic material (linear or nonlinear) and for heterogeneous materials. The conversion to stress intensity factors, however, required an assumption of linear-elastic, homogeneous materials. The formulae are given by [Nishioka (1995), Nishioka, Murakami, and Takemoto (1990)],

$$K_I = \delta_I \sqrt{\frac{2\mu G \beta_{II}}{A_I \left(\delta_I^2 \beta_{II} + \delta_{II}^2 \beta_I \right)}} \tag{14}$$

$$K_{II} = \delta_{II} \sqrt{\frac{2\mu G \beta_I}{A_{II} \left(\delta_I^2 \beta_{II} + \delta_{II}^2 \beta_I \right)}} \tag{15}$$

where μ is the shear modulus, δ_I and δ_{II} denote crack opening and shearing displacements near the crack tip, and β_I, β_{II}, A_I, and A_{II} are parameters related to crack propagation velocity C. They are given by,

$$\beta_I = \sqrt{1 - C/C_s^2} \quad \text{and} \quad \beta_{II} = \sqrt{1 - C/C_d^2} \tag{16}$$

and

$$A_I = \frac{\beta_I (1 - \beta_{II}^2)}{4\beta_I \beta_{II} - (1 + \beta_{II}^2)^2} \tag{17}$$

$$A_{II} = \frac{\beta_{II} (1 - \beta_{II}^2)}{4\beta_I \beta_{II} - (1 + \beta_{II}^2)^2} \tag{18}$$

where C_s and C_d are the shear and dilational wave speeds

$$C_s^2 = \frac{\mu}{\rho} \quad \text{and} \quad C_d^2 = \left(\frac{\kappa + 1}{\kappa - 1} \right) \frac{\mu}{\rho} \tag{19}$$

For a stationary crack with $C = 0$ (all examples in this paper), $\beta_I = \beta_{II} = 1$ and

$$\lim_{C \to 0} A_I = \lim_{C \to 0} A_{II} = \frac{\kappa + 1}{4} \tag{20}$$

In the above equations, $\kappa = (3 - \nu)/(1 + \nu)$ for plane stress and $\kappa = 3 - 4\nu$ for plane strain, where ν is Pois-

son's ratio. These limits lead to

$$K_I = \frac{\delta_I}{\delta}\sqrt{GE} \quad \text{(plane stress)}$$
$$= \frac{\delta_I}{\delta}\sqrt{\frac{GE}{1-\nu^2}} \quad \text{(plane strain)} \qquad (21)$$
$$K_{II} = \frac{\delta_{II}}{\delta}\sqrt{GE} \quad \text{(plane stress)}$$
$$= \frac{\delta_{II}}{\delta}\sqrt{\frac{GE}{1-\nu^2}} \quad \text{(plane strain)} \qquad (22)$$

where E is tensile modulus and δ is the magnitude of the crack opening displacement.

The new MPM results needed for stress intensity factor are the crack opening displacements, δ_I and δ_{II}. The crack opening displacements were calculated from the extension to CRAMP described in the previous section for tracking positions of the crack surfaces. The crack is discretized into a series of massless points connected by segments. The last point defines the crack tip. The last segment defines the crack orientation, θ_c. The crack opening displacements were calculated using the crack surface positions of the next to last point. These opening displacements were resolved into displacement components normal and transverse to the last crack segment to provide δ_I and δ_{II}, respectively; the partitioning only depends on the ratio δ_I/δ_{II}.

4 Results and Discussion

4.1 Static Results

The J-integral calculations and stress intensity factor partitioning were first verified by comparison to static results. Under static conditions, the J-integral calculation is path independent and it is easy to find analytical results for comparison. Figure 4 shows the analysis geometry for two static beam specimens. The specimens were loaded at time zero with loads per unit thickness, P_T and P_B, applied to the top and bottom beams. This geometry results in a pure mode I loading, double cantilever beam specimen (DCB) when $P_B = -P_T$ or a pure mode II loading, end-notch flexure specimen (ENF) when $P_B = P_T$. The material was assumed to be isotropic, linear elastic with a modulus of $E = 2300\,\text{MPa}$ and a Poisson's ratio of $\nu = 0.33$. The specimens were 100 mm long, 24 mm high, and 1 mm thick, and analyzed in plane-stress conditions. All the specimens were clamped on the left edge.

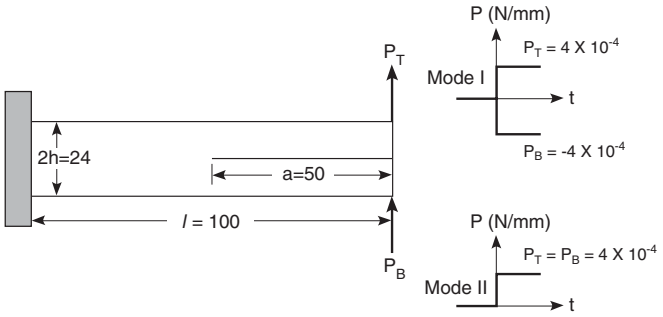

Figure 4 : The geometry of beam specimens used to compare MPM results to static results. By varying P_T and P_B, this specimen can be pure mode I (DCB), pure mode II (ENF), or mixed mode. The loads were applied instantaneously at time zero and then held constant.

The mass density was $\rho = 1.5\,\text{g/cm}^3$. In order to compare the results of stress intensity evaluated by MPM with static results, external damping was incorporated in the computations and adjusted to make the dynamic vibrations damp out after a few oscillations. The damped out results should converge to the static solution. The damping coefficient in Eq. 1 for these specimens was set to $d_k = 1000\,\text{sec}^{-1}$. To test convergence, the dimensions of the background mesh cells for both the DCB and ENF specimens were varied from $4 \times 4\,\text{mm}$ down to $1 \times 1\,\text{mm}$. For all meshes, there were 4 particles per cell. The initial spacing between particles thus varied from 2 mm to 0.5 mm or 4% to 1% of the crack length (50 mm). The J-integral contour was 2×2 cells. The distance of the contour to the crack tip thus varied from 8 mm to 2 mm or 16% to 4% of the crack length.

Figures 5 and 6 compare the results of dynamic stress intensity evaluated by MPM to the static results. For the DCB specimen, the static stress intensity factors were found using corrected beam theory [Kanninen (1973)]:

$$K_{Is} = 2\sqrt{3}\frac{P_T(a+\chi h)}{h^{3/2}} \quad \text{and} \quad K_{IIs} = 0 \qquad (23)$$

where χ is a correction factor to account for crack-root rotation effects and $\chi = 2/3$ for isotropic materials. For the ENF specimen, the static stress intensity factors were found from [Carlsson, Gillespire, and Pipes (1986), Guo and Tang (1993)]:

$$K_{Is} = 0 \text{ and } K_{IIs} = \frac{3P_T a}{h^{3/2}}\sqrt{1+\frac{2(1+\nu)}{5}\left(\frac{h}{a}\right)^2} \qquad (24)$$

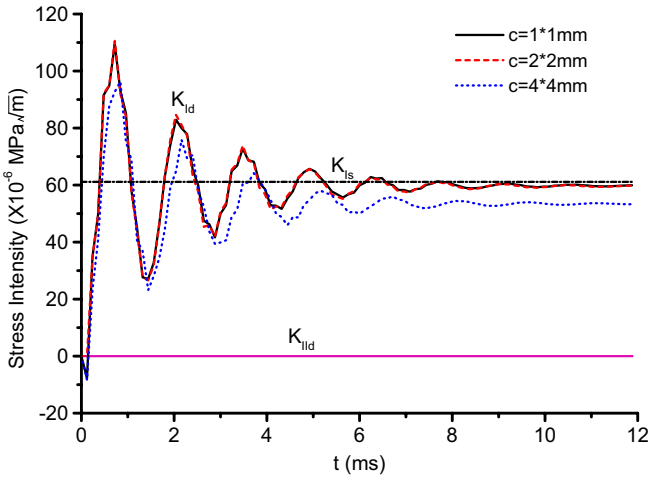

Figure 5 : Comparison of the stress intensity factors, K_I and K_{II}, for the DCB beam specimen calculated by MPM analysis using three different cell sizes or by analytical results (horizontal line). The dynamic MPM results had damping such that they should converge to the static solution.

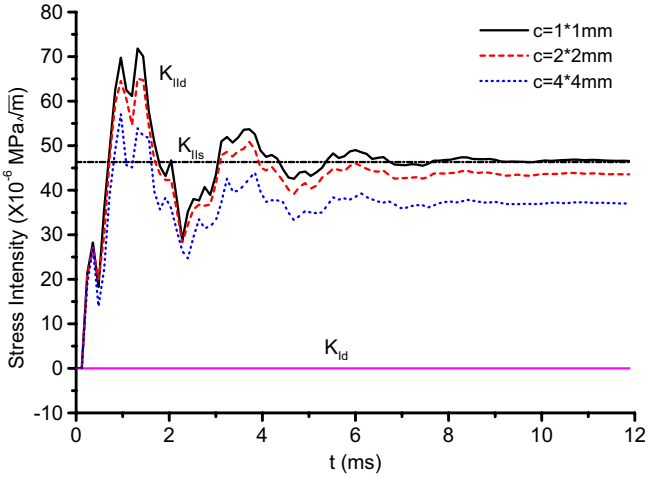

Figure 6 : Comparison of the stress intensity factors, K_I and K_{II}, for the ENF beam specimen calculated by MPM analysis using three different cell sizes or by analytical results (horizontal line). The dynamic MPM results had damping such that they should converge to the static solution.

For both the DCB and ENF specimens, the converged MPM results oscillated around the analytical results and converged to those results when damping was complete. The mode I results converged for 2×2 mm cells, while the mode II results required smaller 1×1 mm cells. The correct partitioning of energy release rate into K_I and K_{II} is shown by the calculation of $K_{II} = 0$ for the DCB specimen (Fig. 5) and $K_I = 0$ for the ENF specimen (Fig. 6). The partitioning was further verified by analysis of mixed-mode specimens such as using $P_T = P$ and $P_B = 0$.

4.2 Dynamic Results

Three specimens were used to compare the results of stress intensity factors evaluated by MPM through J-integral to the results computed by other approaches. The first two specimens were a central cracked tension (CCT) specimen and a single edge notched tension (SENT) specimen. Figures 7a and 7b show the geometry and the axial Heaviside load boundary condition for these specimens. They were analyzed under plane strain conditions. The crack-tip loading was pure mode I. The material was linear elastic with a modulus of $E = 200$ GPa and Poisson's ratio of $\nu = 0.3$. The mass density of the material was set to $\rho = 5.0\,\mathrm{g/cm^3}$. The dimensions of the specimens and the crack lengths are given in Fig. 7. The dimensions of background mesh cells were 0.5×0.5 mm with 4 particles per cell. The particle spacing was thus 0.25 mm which is 1.25% of the specimen width, 5.2% of the CCT crack length, and 5% of the SENT crack length. The J-integral contour was 2×2 cells.

Figures 8 and 9 compare the results of dynamic mode I stress intensity factors of the CCT and SENT specimens calculated by MPM to prior results calculated by the finite difference method [Chen and Wilkens (1977)]. In the two figures, the stress intensity factors were normalized by the static, infinite-sheet stress intensity factor of $K_{I0} = \sigma_0\sqrt{\pi a}$ where $\sigma_0 = 400$ MPa is the value of the applied stress, and a is 2.4 mm and 5 mm for the CCT and SENT specimens, respectively. Figures 8 and 9 show that the new results calculated by MPM agree well with prior numerical results.

The third dynamic specimen analyzed was a double edge notched plate (DENP) specimen dynamically loaded in impact compression between the two notches (see Fig. 7c). The DENP specimen has been used as an impact specimen to study the dynamic fracture toughness under shear or mode II loading [Kalthoff and Winkler (1987)]. Although analysis shows the loading is mostly mode II, the mode I component is non-zero or the loading is actually mixed mode. The material was linear elastic with a modulus of $E = 210$ GPa and Poisson's ratio of $\nu = 0.29$

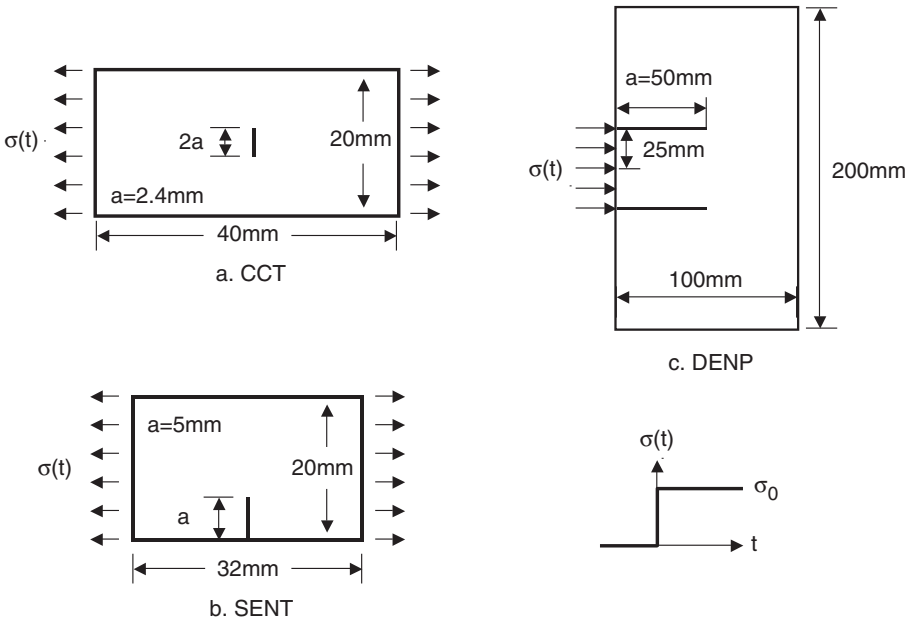

Figure 7 : Specimen geometries for dynamic stress intensity factor calculations. a. Center crack tension (CCT) specimen. b. Single edge notched tension (SENT) specimen. c. Double edge notched plate (DENP) specimen. All specimens where loaded (as indicated by arrows) instantaneously at time zero and then the stress was held constant.

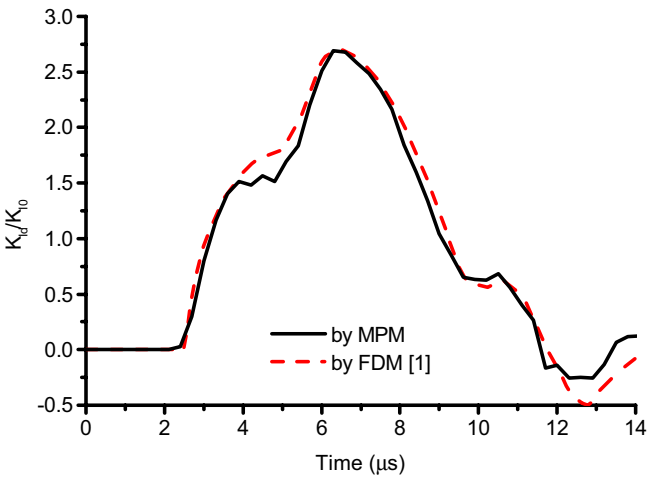

Figure 8 : Comparison of the mode I stress intensity factor (K_I) for the CCT specimen calculated by MPM or by finite difference method (FDM in Chen and Wilkens (1977)).

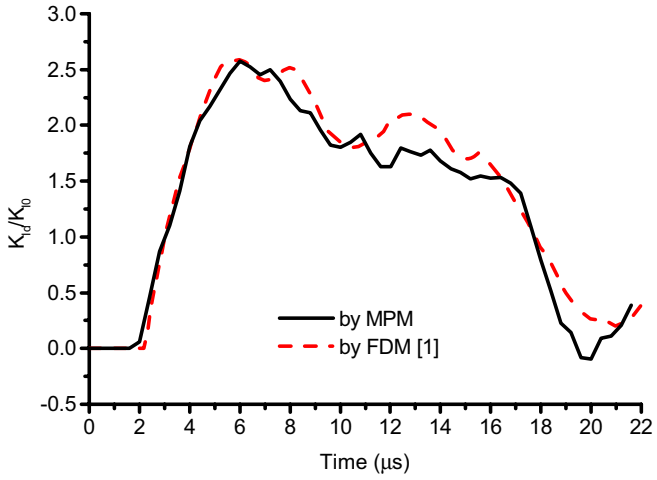

Figure 9 : Comparison of the mode I stress intensity factor (K_I) for the SENT specimen calculated by MPM or by finite difference method (FDM in Chen and Wilkens (1977)).

and analyzed under plane-strain conditions. The impact compression stress was $\sigma_0 = 200\,\text{MPa}$. The mass density of the material was set to $\rho = 7.833\,\text{g/cm}^3$. The dimensions of the specimens and the crack lengths are given in Fig. 7c. The dimensions of the background mesh cells were $2 \times 2\,\text{mm}$ with 4 particles per cell. The particle spacing was thus 1 mm which is 1% of the specimen width and 2% of the crack length. The J-integral contour was 2×2 cells. The MPM calculations used symmetry and analyzed only the top half of the specimen. The nodal velocities in the y direction in the midplane of the specimen were constrained to zero to define the symme-

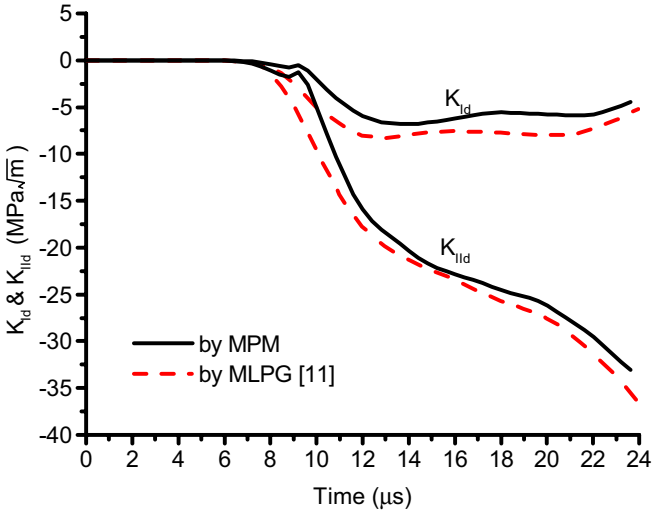

Figure 10 : Comparison of the mode I and mode II stress intensity factors (K_I and K_{II}) for the DENP specimen calculated by MPM or by Meshless Local Petrov Galerkin (MLPG in Batra and Ching (2002)) method.

try plane.

Figure 10 compares the results of mode I and mode II stress intensity factors evaluated by MPM to prior results calculated by the Meshless Local Petrov-Galerkin (MLPG) method [Batra and Ching (2002)]. The two methods have similar results. The slight differences may be a real difference because the MPM results and MLPG results were for slightly different problems. The MLPG analysis used highly refined particle density near the crack tip in an attempt to resolve the effect of the actual machined crack tip with a radius of 0.15 mm [Batra and Ching (2002)]. The MPM analysis assumed a sharp crack, although at the analyzed resolution, the MPM results would not distinguish crack radii less than the half the inter-particle spacing (0.5 mm). The MPM results could be extended to higher resolution, but the similarity of the results in Fig. 10 indicates the details on the crack tip shape do not have a large effect provided the crack is reasonably sharp (< 0.5 mm).

4.3 Path Effects on Dynamic J Integral

The results in the previous section were for small rectangular paths (see Fig. 3) that extended 2 cells in the x and y directions from the node nearest to the crack tip (2×2 cell paths). The distance from the crack tip to these contours was 8% of the crack length for most specimens, but was 20% of the crack length for the CCT and DENP specimens. These contours were judged to be sufficiently small (by comparison to other methods), that the J-integral could be evaluated by Eq. 7. In other words, J-integral was evaluated by the first term in Eq. 8 and the second term was assumed to be negligible. The advantage of this approach is numerical efficiency because the extrapolations and calculations needed for the second term could be skipped. For calculations using larger contours or for different problems with different dynamic effects, the second term might be needed. This section describes some calculations for a problem where the second term is needed and shows it can be evaluated by MPM.

We repeated the DENP calculations for a rectangular paths from 2×2 cells up to 10×10 cells. The later was the largest square path that could be accommodated in the DENP specimen and remain within the material when using cells that were 2×2 mm. For small contours (under 5×5 cells), the second term in Eq. 8 was negligible and thus Eq. 7 was accurate for calculating the J-integral. For larger paths, however, the differences became significant. Figure 11 compares mode II stress intensity factors calculated by the smallest and largest paths either with or without the second term in Eq. 8. The lack of difference for the two 2×2 cells path results verifies the second term was negligible for that size path. In contrast, the second term has a large effect on the 10×10 cells path results. When the second term was ignored, the large path give poor results. The oscillations correspond to stress waves passing through the contour. When the second term was included, the large path calculation agreed with the small path calculations for most times. This result shows that MPM can evaluate the second term and that analysis using both terms in Eq. 8 gives a path-independent result.

There are discrepancies between the small path and the two-term, large path results for times less than about 9 μs. This time corresponds to the time required for the stress initiated by the impact loading to travel from the edge of the specimen to the crack tip. Thus, the results for times less than 9 μs correspond to times for which stress waves have reached the J-integral contour, but have not yet reached the crack tip. The results in this region are probably more reliable with the smaller path. The recommendation is that all MPM calculations of J integral should use a small path. The second term may be included to insure path independence, but it will probably

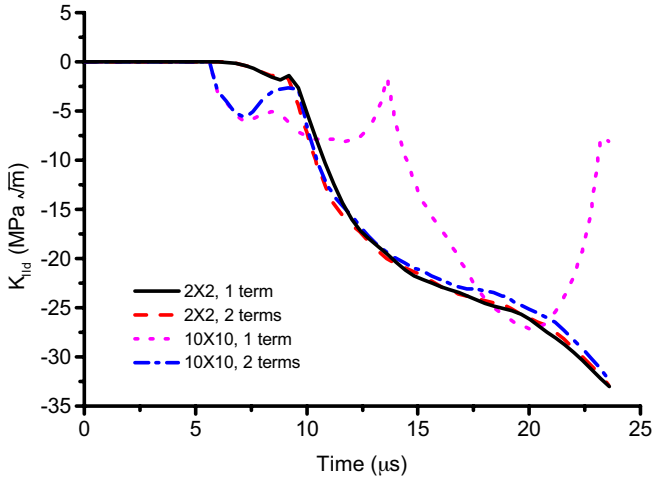

Figure 11 : Calculation of J integral using a line integral (one term or Eq. 7) or using a line and and area integrals (two terms or Eq. 8). The calculations were for a small contour (2×2 cells) or for a large contour (10×10 cells). The results are for the mode II stress intensity factor (K_{II}) in a DENP specimen

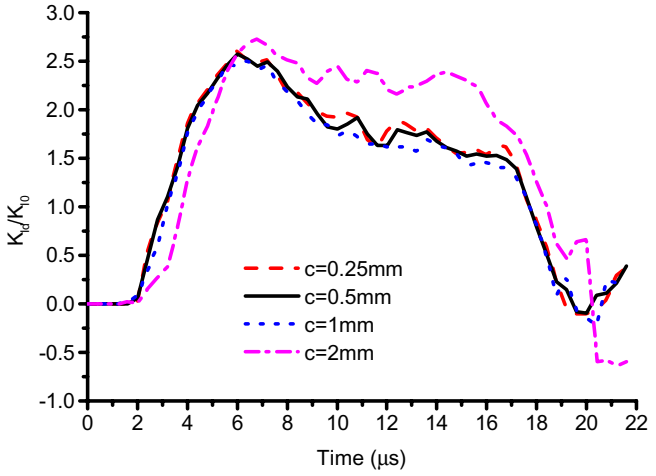

Figure 12 : Calculation of the mode I stress intensity factor (K_I) in an SENT specimen as a function of the background mesh density. All calculations used a rectangular path that extend two cells from the crack tip in each direction. The background cells sizes, however, were varied using $c = 0.25$ mm, $c = 0.5$ mm, $c = 1.0$ mm, or $c = 2.0$ mm.

be negligible for typical problems.

4.4 *Effect of Background Mesh Size on Stress Intensity Factor*

The stress intensity factors were computed here by converting J-integral results rather than by direct evaluation from local crack-tip stresses and displacements. Because the J-integral calculations work well, even for relatively crude meshes, it is reasonable to expect that the calculation of stress intensity in MPM can be accurate and more computationally effective than in direct methods, which might require finer meshes. In dynamic analysis, computational efficiency is extremely important because an enormous number of time steps are often required for typical problems. The use of a relatively coarse background mesh, while still obtaining good J-integral results, would save a great deal of computational time. This section describes calculations to assess the computational efficiency of dynamic J-integral in MPM, *i.e.*, to assess the tolerance of the calculation to large background cell sizes.

We repeated the SENT calculations (see Fig. 9), which previously had cell size of $c = 0.5$ mm or 0.5 by 0.5 mm cells, with background meshes having $c = 0.25$ mm, $c = 1.0$ mm, and $c = 2.0$ mm. For a crack length of 5 mm, a specimen width of 20 mm, and four particles per cell, these cell sizes correspond to inter-particle spacings ($s = c/2$) that are 2.5%, 5%, 10%, and 20% of the crack length (a) and 0.625%, 1.25%, 2.5%, and 5% of the specimen width (W). The J-integral contours were chosen along grid line segments two cells away from the crack tip in both the x and y directions. The normalized mode I stress intensity factors for each cell size are plotted in Fig. 12.

The results in Fig. 12 show that the J-integral results converge for the relatively coarse mesh of $c = 1$ mm, which corresponds to relative mesh size of $s/a = 10\%$ and $s/W = 2.5\%$. The results for all finer meshes were nearly identical. The results for the coarsest mesh ($c = 2$ mm) showed deviations or lost accuracy. The ability to obtain accurate J-integral results without the need for highly refined crack-tip meshes is especially important in dynamic problems because each factor of 2 in cell size leads to a factor of $2^3 = 8$ (in 2D or $2^4 = 16$ in 3D) increase in calculation time. There is a factor of two for each dimension and another factor of two because smaller meshes require proportionally smaller times steps in explicit solvers. The ability to find accurate J-integral when $c = 1.0$ mm instead of needing $c = 0.25$ mm provides a factor 64 (in 2D) or 256 (in 3D) efficiency in crack problems.

5 Conclusions

The material point method is a new method that has interesting potential for handling fracture problems involving crack propagation. MPM has previously been extended to allow analysis of problems with explicit cracks [Nairn (2003)]. It can include explicit cracks with the ease of finite element analysis while retaining the advantages of meshless methods for the ease of handling crack propagation in arbitrary directions. This paper has described new MPM algorithms for calculating J-integral and for partitioning the total energy release rate into mode I and mode II stress intensity factors. Several examples were considered and all show that MPM results agree with analytical solutions or with prior numerical results. Although calculations of dynamic J-integral, can usually be calculated by Eq. 7 using a small path around the crack tip, true path-independent results require the line integral to be supplemented with an area integral inside the contour as in Eq. 8. MPM can find J integral by either approach and both have computational efficiency. The area integral can be found by using the particles enclosed in the contour as integration points. Finally, some convergence tests suggest that J-integral calculations are accurate even with fairly coarse meshes. The introduction outlined three key problems to numerical analysis of dynamic fracture. The results in Nairn (2003) and the results in this paper show that MPM can solve the first two problems. Future work should be aimed at the third problem or full MPM analysis of fracture problems including crack propagation.

Acknowledgement: This work was supported by a grant from the Department of Energy DE-FG03-02ER45914 and by the University of Utah Center for the Simulation of Accidental Fires and Explosions (C-SAFE), funded by the Department of Energy, Lawrence Livermore National Laboratory, under Subcontract B341493.

References

Atluri, S. N.; Shen, S. (2002): The Meshless Local Petrov-Galerkin (MLPG) method: A Simple & Less-Costly Alternative to the Finite Element and Boundary Element Methods. *CMES: Computer Modeling in Engineering & Sciences*, vol. 3, pp. 11–52.

Bardenhagen, S. G.; Brackbill, J. U.; Sulsky, D. (2000): The Material Point Method for Granular Materials. *Computer Methods in Applied Mechanics and Engineering*, vol. 187, pp. 529–541.

Bardenhagen, S. G.; Guilkey, J. E.; Roessig, K. M.; Brackbill, J. U.; Witzel, W. M.; Foster, J. C. (2001): An Improved Contact Algorithm for the Material Point Method and Application to Stress Propagation in Granular Material. *CMES: Computer Modeling in Engineering & Sciences*, vol. 2, pp. 509–522.

Bardenhagen, S. G.; Kober, E. M. (2004): The Generalized Interpolation Material Point Method. *CMES: Computer Modeling in Engineering & Sciences*, vol. 5, pp. 477–496.

Batra, R. C.; Ching, H.-K. (2002): Analysis of Elastodynamic Deformations Near a Crack/Notch Tip by the Meshless Local Petrov- Galerkin (MLPG) Method. *CMES: Computer Modeling in Engineering & Sciences*, vol. 3, pp. 717–730.

Belytschko, T.; Lu, Y. Y.; Gu, L. (1994): Element-Free Galerkin Methods. *Int. J. Num. Meth. Engrg.*, vol. 37, pp. 229–256.

Carlsson, L. A.; Gillespire, J. W.; Pipes, R. B. (1986): On The Analysis and Design of The End Notched Flexure (ENF) Specimen for Mode II Testing. *J. Comp. Mater.*, vol. 20, pp. 594–604.

Chen, Y. M.; Wilkens, M. L. (1977): *Numerical Analysis of Dynamic Crack Problems*, pp. 317–325. In *Elastodynamic Crack Problems*, Noordhoff International Publishing, The Netherlands, 1977.

Cherepanov, G. P. (1967): The Propagation of Cracks in A Continuous Media. *J. Appl. Math. Mech.*, vol. 31, pp. 503–512.

Cherepanov, G. P. (1979): *Mechanics of Brittle Fracture*. McGraw-Hill, New York.

Cook, R. D.; Malkus, D. S.; Plesha, M. E. (1989): *Concepts and Applications of Finite Element Analysis*. John Wiley & Sons, New York.

Ferretti, E. (2003): Crack Propagation Modeling by Remeshing Using the Cell Method (CM). *CMES: Computer Modeling in Engineering & Sciences*, vol. 4, pp. 51–72.

Guo, Y.; Nairn, J. A. (2004): Three-Dimensional Dynamic Fracture Analysis in the Material Point Method. In preparation, 2003.

Guo, Y. J.; Tang, J. M. (1993): Finite Element Analysis of Strain-Energy-Release Rate for The End Notched Flexure (ENF) Specimen. In *Proc. 38th Int. SAMPE Symp. & Exhibition*, pp. 857–867.

Han, Z. D.; Atluri, S. N. (2003): SGBEM (for Cracked Local Subdomain) FEM(for uncracked global Structure) Alternating Method for Analyzing 3D Surface Cracks and Their Fatigue-Growth. *CMES: Computer Modeling in Engineering & Sciences*, vol. 3, pp. 699–716.

Han, Z. D.; Atluri, S. N. (2003): Truly Meshless Local Petrov-Galerkin (MLPG) Solutions of Traction & Displacement BIEs. *CMES: Computer Modeling in Engineering & Sciences*, vol. 4, pp. 665–678.

Kalthoff, J. F.; Winkler, S. (1987): Failure Mode Transition at High Rates of Shear Loading. In *Proc. Int. Conf. on Impact Loading and Dynamic Behaviour of Materials*, pp. 185–195.

Kanninen, M. F. (1973): An Augmented Double Cantilever Beam Model for Studying Crack Propagation and Arrest. *Int. J. Fract.*, vol. 9, pp. 83–92.

Nairn, J. A. (2003): Material point method calculations with explicit cracks. *Computer Methods in Applied Mechanics and Engineering*, vol. 4, pp. 649–664.

Nishioka, T. (1983): A Numerical Study of the Use of Path Independent Integrals in Elastic-Dynamic Crack Propagation. *Engr. Fract. Mech.*, vol. 18, pp. 23–33.

Nishioka, T. (1995): *Recent Developments in Computational Dynamic Fracture Mechanics*, pp. 1–58. In *Dynamic Fracture Mechanics*, Computational Mechanics Publications, Southampton, UK, 1995.

Nishioka, T. (1997): Computational Dynamic Fracture Mechanics. *Int. J. Fract.*, vol. 86, pp. 127–159.

Nishioka, T.; Atluri, S. N. (1983): Path-Independent Integrals, Energy Release Rates, and General Solutions of Near-Tip Fields in Mixed-Mode Dynamic Fracture Mechanics. *Engr. Fract. Mech.*, vol. 18, pp. 1–22.

Nishioka, T.; Murakami, R.; Takemoto, Y. (1990): The Use of The Dynamic J Jntegral (J) in Finite-Element Simulation of Mode I and Mixed-Mode Dynamic Crack Propagation. *International Journal of Pressure Vessels and Piping*, vol. 44, pp. 329–352.

Nishioka, T.; Stan, F. (2003): A Hybrid Experimental-Numerical Study on the Mechanism of Three-Dimensional Dynamic Fracture. *CMES: Computer Modeling in Engineering & Sciences*, vol. 4, pp. 119–140.

Nishioka, T.; Tokudome, H.; Kinoshita, M. (2001): Dynamic Fracture-Path Prediction in Impact Fracture Phenomena Using Moving Finite Element method based on Delaunay Automatic Mesh Generation. *Int. J. Solids Struct.*, vol. 38, pp. 5273–5301.

Organ, D. J.; Fleming, M.; Belytschko, T. (1996): Continuous Meshless Approximations for Nonconvex Bodies by Diffraction and Transparency. *Computational Mechanics*, vol. 18, pp. 225–235.

Rice, J. R. (1968): A Path Independent Integral and the Approximate Analysis of Strain Concentration by Notches and Cracks. *J. Applied Mech.*, vol. June, pp. 379–386.

Rybicki, E. F.; Kanninen, M. F. (1977): A Finite Element Calculation of Stress Intensity Factors By a Modified Crack Closure Integral. *Eng. Fract. Mech.*, vol. 9, pp. 931–938.

Sulsky, D.; Chen, Z.; Schreyer, H. L. (1994): A Particle Method for History-Dependent Materials. *Comput. Methods Appl. Mech. Engrg.*, vol. 118, pp. 179–186.

Sulsky, D.; Schreyer, H. K. (1996): Axisymnmetric Form of the Material Point Method with Applications to Upsetting and Taylor Impact Problems. *Comput. Methods. Appl. Mech. Engrg*, vol. 139, pp. 409–429.

Sulsky, D.; Zhou, S.-J.; Schreyer, H. L. (1995): Application of a Particle-in-Cell Method to Solid Mechanics. *Comput. Phys. Commun.*, vol. 87, pp. 236–252.

Tan, H.; Nairn, J. A. (2002): Hierarchical Adaptive Material Point Method in Dynamic Energy Release Rate Calculations. *Comput. Meths. Appl. Mech. Engrg.*, vol. 191, pp. 2095–2109.

Wen, P. H.; Aliabadi, M. H.; Rooke, D. P. (1998): Cracks in Three Dimensions: A Dynamic Dual Boundary Element Analysis. *Comput. Methods Appl. Mech. Engrg*, vol. 167, pp. 139–151.